Nitrogen and carbon isotope composition of the ca. 1.33 Ga phosphorite (South Urals): Evidence for transient deep-water oxygenation?

Eva E. Stüeken[1,*], Anton B. Kuznetsov[2],
Irina M.Vasilyeva[2], Mikhail T.Krupenin[3], Andrey Bekker[4,5]

1. School of Earth & Environmental Sciences, University of St Andrews, Irvine Building, North Street, St Andrews, Fife, KY16 9AL, Scotland, UK
2. Institute of Precambrian Geology and Geochronology, Russian Academy of Sciences, Makarova nab., 2, St. Petersburg 199034, Russia
3. Institute of Geology and Geochemistry, Russian Academy of Sciences, Ural Branch, Russian Academy of Sciences, Yekaterinburg, 620016 Russia
4. Department of Earth and Planetary Sciences, University of California, Riverside, Riverside, CA 92521, USA
5. Department of Geology, University of Johannesburg, Auckland Park 2006, South Africa

* corresponding author (ees4@st-andrews.ac.uk)

Published in *Precambrian Research, 360,* 106242

Abstract

The Mesoproterozoic deep-ocean is thought to have been largely anoxic, dominated by ferruginous conditions, with iron oxyhydroxides scavenging phosphate from the water column, and suppressed accumulation of dissolved nitrate. Primary productivity was therefore generally low, and eukaryotic life was restricted to oxic marine margins. This model is supported by new nitrogen isotope data from the Lower Riphean (ca. 1.55 Ga) strata of the South Ural Mountains, where we find evidence for strong redox stratification, coupled with low organic carbon contents. In contrast, unconformably overlying siliciclastic sediments of the Middle Riphean age (ca. 1.33 Ga) preserve a rare occurrence of phosphate concretions, associated with relatively high concentrations of organic carbon (up to 4 wt. %). The Pb-Pb isochron age for phosphate nodules of the Zigazino-Komarovo Formation is 1330 ± 20 Ma (MSWD = 3.7). We measured nitrogen isotope ratios across this interval and found $\delta^{15}N$ values up to +7.6‰, which are similar to those in modern upwelling zones and indicative of a significant nitrate reservoir. These observations are most parsimoniously explained by upwelling of phosphate- and nitrate-bearing waters, suggesting that the deep ocean was at least regionally and temporarily oxygenated. The lack of redox-sensitive trace element enrichment in these strata and the general scarcity of phosphate accumulations in the Mesoproterozoic sedimentary records suggest that oxic deep-waters were not a global and persistent phenomenon, but our results confirm that oxic, nutrient-rich refugia existed in the Mesoproterozoic oceans and were perhaps important for the radiation of early eukaryotes.

1. Introduction

Nitrogen (N) and phosphorus (P) are the two major bio-limiting nutrients for primary productivity in the modern ocean (Redfield, 1934; Gruber & Deutsch, 2014) and have been suggested to be potentially responsible for the delay in radiation of eukaryotic life on the early Earth (Anbar & Knoll, 2002; Stüeken, 2013; Kipp & Stüeken, 2017; Reinhard *et al.*, 2017). In the modern oxic ocean, both N and P display nutrient-type profiles that are characterised by (a) depletion in the photic zone caused by biological uptake, and (b) relatively elevated concentrations in the deep ocean due to remineralization of organic matter (Sverdrup *et al.*, 1942). Upwelling of deep waters to the surface ocean is therefore an important mechanism for replenishing the nutrient supply of primary producers. Upwelling zones develop along continental margins, driven by large-scale ocean and atmospheric circulation. Today, these zones typically display oxygen depletion at mid-depth in the water column, because locally elevated primary productivity, fuelled by the supply of nutrients from depth, leads to rapid respiration and oxygen consumption (Karstensen *et al.*, 2008). Regions of coastal upwelling are therefore characterized by high accumulation rates of organic carbon (Premuzic *et al.*, 1982). They also represent prime locations for water-column nitrate reduction (denitrification) (Sigman *et al.*, 2009; Lam & Kuypers, 2011) as well as for the formation of economic phosphate deposits (Pufahl & Groat, 2017). Where upwelling occurs along the edge of epicontinenal basins, phophorite deposition can extend well onto the continental platform (Pufahl & Groat, 2017). Phosphogenesis is thought to be driven by sulphide-oxidizing bacteria, which have been shown to accumulate phosphate within their cells and release it to pore-waters under anoxic conditions (Schulz & Schulz, 2005). These organisms thrive in modern upwelling zones, because they are adapted to the fluctuating redox conditions that commonly occur in regions of high productivity. Importantly, the high degree of primary as well as secondary productivity can only be sustained there because upwelling water masses from the deep ocean are enriched in nitrate and phosphate in today's oxic world.

In the Precambrian, the deep ocean was largely ferruginous, *i.e.* anoxic with freely dissolved ferrous iron (Poulton & Canfield, 2011; Sperling *et al.*, 2015). Under these conditions, phosphate was scavenged from the water column, because it was readily incorporated into ferrous phosphate minerals and green rust (Reinhard *et al.*, 2017) and it also co-precipitated with Fe-(oxyhydr)oxides above a redoxcline in coastal upwelling zones where Fe(II) was oxidized (Bjerrum and Canfield, 2002; Laakso and Schrag, 2014; Jones et al., 2015). Furthermore, recycling of organic-bound P and N was suppressed when electron acceptors were less abundant and largely unavailable in the deep ocean for efficient remineralization of organic matter (Kipp & Stüeken, 2017). Recycled N would therefore have been in the form of ammonium rather than nitrate. Upwelling zones almost certainly existed, similar to today's oceans, but the upwelling water masses would likely have been less nutrient-rich, and more oxygen-depleted and iron- and manganese-rich, enhancing oxygen-consumption and sulphate reduction in surface waters. Occurrence of euxinic (H_2S-rich) waters along continental margins in several Proterozoic basins may be an expression of coastal upwelling at that time (Poulton *et al.*, 2010; Lyons *et al.*, 2014).

This model is consistent with the scarcity of sedimentary P accumulations in the Mesoproterozoic (Papineau, 2010), because dissolved P concentrations in upwelling deep waters were likely too low to produce notable phosphorite deposits. Paleoproterozoic phosphorites, possibly associated with deepening of the redoxcline in the water column during the time of atmospheric oxygenation, Great Oxidation Event (GOE), (Lepland *et al.*, 2014; Hiatt *et al.*, 2015; Kipp *et al.*, 2020), are an important case in point. A global expansion of phosphorite deposition occurred in the latest Neoproterozoic to earliest Cambrian,

accompanied by progressive ventilation of the deep ocean. Upwelling, in association with intense continental weathering, probably led to widespread phosphogenesis on several Neoproterozoic continents in large epicontinental basins such as Georgina, Himalaya, Yangtze, Karatau, Khubsugul-Bokson, and Volta (e.g., Chaudhuri, 1980; Cook, 1992; Kholodov, 1997; Ilyin, 1998; Chen *et al.*, 2004; Kuznetsov *et al.*, 2018). The economically important, stromatolitic phosphorite deposits of the ~1.7 Ga Aravalli Group in Rajasthan, India stand as a notable exception to this trend (McKenzie et al., 2013).

However, phosphorite occurrences are extremely rare in the Mesoproterozoic (Cook and McElhinny, 1979; Kholodov, 1997, 2002), and where they occur, they might represent biogeochemical perturbation in seawater's chemistry and redox state. A rare example of Mesoproterozoic phosphate accumulation has been documented in Mesoproterozoic organic-rich sedimentary rocks of the South Ural Mountains (Ovchinnikova *et al.*, 2013). Here phosphate enrichment occurs at two thin horizons. The first is a phosphate cement within stromatolitic domes at the base of the 1550 ± 30 Ma Satka Formation in the Early Riphean Burzyan Group (1550 ± 30 Ma, Kuznetsov *et al.*, 2008). The meter-size dome bears extensively developed quartz veins related to severe hydrothermal alteration (Ovchinnikova *et al.*, 2008). The second, better-preserved horizon, which was investigated in this study, occurs within a package of black shales and siltstones in the lowest part of the Zigazino-Komarovo Formation of the Middle Riphean Yurmatau Group. Preliminary Pb-Pb dating of the latter phosphate has yielded an age of 1330 ± 20 Ma (Ovchinnikova *et al.*, 2013). The Zigazino-Komarovo Formation was deposited in a nearshore setting above the wave base (Maslov, 1991). The phosphatic horizon in the lower part of the Zigazino-Komarovo Formation is a few meters thick and rests conformably on thin highly pyritiferous black shale. This unit is the most organic-rich (up to 4% organic carbon) portion of the entire Riphean succession of the South Urals (Maslov *et al.*, 1997) and it contains siderite, ankerite, and Fe-rich dolomite lenses (Maslov, 1991). With these characteristics, the phosphatic-pyritic Zigazino-Komarovo Formation resembles modern upwelling zones and therefore offers an opportunity to investigate the effect of upwelling on nutrient level on the Mesoproterozoic open-marine shelves around the time when eukaryotes radiated into the marine realm (Knoll & Nowak, 2017; Sánchez-Baracaldo *et al.*, 2017).

The Middle Riphean Yurmatau Group rests unconformably on the 1430 ± 30 Ma Bakal Formation (1430 ± 30 Ma, Kuznetsov *et al.*, 2005) of the Lower Riphean Burzyan Group. The Bakal Formation is composed of black shales grading into stromatolitic dolostones. The thick black shale interval has been interpreted as deposited in a relatively deep-water setting, whereas the stromatolitic dolostones likely represent shallow-water shelf environment in the photic zone. Organic carbon content is low (<0.5%) and phosphate deposits are lacking throughout the Bakal Formation (Doyle *et al.*, 2018). We will therefore use the Bakal Formation as a regional baseline for the Mesoproterozoic basin that preserves both shallow- and deep-water facies, but does not show evidence of coastal upwelling unlike the Zigazino-Komarovo Formation.

2. Geologic Setting

The Burzyan and Yurmatau groups are developed along the western margin of the South Urals. They represent the stratotype of the Mesoproterozoic Lower and Middle Riphean stratigraphic divisions in Central Russia (Semikhatov *et al.*, 2009; Semikhatov *et al.*, 2015). The strata outcrop on the northeastern and central parts of the Bashkir Anticlinorium (Fig. 1), which was uplifted during the Uralian Orogeny in the Paleozoic (Pushkov, 1997). While the eastern limb of the anticlinorium is highly metamorphosed, the western limb has experienced only burial diagenesis (Maslov *et al.*, 2001; Glasmacher *et al.*, 2004). The

succession is composed of volcano-sedimentary units that were originally deposited along the eastern margin of the Baltica Craton (Maslov, 2004).

The Burzyan Group rests unconformably on the Archean–Paleoproterozoic metamorphic basement and is subdivided into three units (Fig. 1): the Ai Formation (volcanogenic-siliciclastic, 1700–2500 m in thickness), the Satka Formation (shale and carbonate, including siderites, 1700–3500 m thick), and the Bakal Formation (carbonate-siltstone-shale, 1300–1600 m thick). Recently, trachybasaltic porphyrite of the Navysh Subformation of the Ai Formation has been dated by U-Pb SHRIMP zircon method at 1752 ± 11 Ma (Krasnobaev et al., 2013; Puchkov et al., 2014). The minimal age of the Burzyan Group is constrained by the 1385 ± 1.4 Ma U–Pb TIMS baddeleyite age of a diabase dyke crosscutting the Bakal Formation (1385 ± 1.4 Ma, Ernst *et al.*, 2006) and by the 1370 ± 4.6 Ma U–Pb SHRIMP zircon age of rapakivi granite from the Berdyaush Massif intruding the Satka Formation (Ronkin et al., 2007).

The Burzyan Group is unconformably overlain by the Mashak bimodal volcanic unit (basalt-rhyolite, up to 2500 m in thickness), which forms the base of the Middle Riphean Yurmatau Group. In the western part of the Bashkir Anticlinorium, the Mashak volcanics are overlain conformably by conglomerates and sandstones of the 120 to 550 m thick Zigalga Formation. The Zigalga Formation is in turn overlain by the siliciclastic, 600 to 1200 m thick Zigazino–Komarovo Formation and then by the mixed, siliciclastic-carbonate, 400 to 900 m thick Avzyan Formation. Deposition of the Yurmatau Group started with the Mashak volcanics, which contain dacites dated at 1370 ± 16 Ma by U-Pb SHRIMP zircon method (Ronkin *et al.*, 2007).

Geodynamic reconstructions suggest that the Riphean Bashkir basin formed as a consequence of rifting at the beginning of the Early Riphean (ca. 1.75 Ga) and was reactivated into a broad passive continental margin at ca. 1370 Ma (Maslov *et al.*, 1997; Maslov, 2004; Semikhatov *et al.*, 2015). Both the Burzyan and Yurmatau groups (Fig. 1) start with mafic (basalts) to intermediate volcanics, followed by fluvial conglomerates and sandstones that stratigraphically higher transition to shallow-marine carbonates, shales and siltstones (Maslov *et al.*, 1997). This first-order lithological sequence is interpreted as an overall upward-deepening trend.

The Satka Formation of the Burzyan Group is composed of stromatolitic and massively bedded dolostones, flat-pebble dolostones, marls, shales, fine siltstones and laminated limestone. The base of the Satka Formation contains stromatolitic domes with scattered phosphate cement between and within columns (Fig. 2a). As noted above, we did not study this unit because it shows evidence of alteration in the form of cross-cutting quartz veins. Based on sedimentary structures, the Satka Formation siliciclastic facies are interpreted as sub-storm wave-base deposits (Fig. 2b), while the carbonates were likely deposited between storm and fairweather wave-base (Doyle *et al.*, 2018). The overlying Bakal Formation consists of six members: Makar-Bereza, Irkuskan, Shuida, Gaev, Shikhan and Bulandikha (Krupenin, 1999), which correspond to six cycles grading from gray to black shales at the base to columnar stromatolitic carbonates at the top (Semikhatov *et al.*, 2009) (Fig. 2c). This succession probably represents an upward-shallowing trend. The Bashkir basin was likely somewhat restricted during this time, but tidal indicators and Sr isotope data point towards an open-marine connection (Kuznetsov *et al.*, 2005; Kuznetsov *et al.*, 2008; Semikhatov *et al.*, 2009).

The overlying coarse-grained siliciclastic sediments of the Zigalga Formation represent a braided fluvial system, while the cross-bedded quartz sandstones and black shales of the Zigazino-Komarovo Formation (Fig. 2h) were likely deposited above fair-weather wave-base in a protected coastal plain setting, similar to that of the modern Wadden Sea. The Zigazino-Komarovo Formation consists of three subformations: Seregin, Ambarka and

Tukan, with the total thickness of 750 to 1200-1500 meters (Maslov, 1991). The grey- to black-coloured Seregino Subformation contains beds of black shales and siltstones with pyrite nodules (up to 4 cm in diameter) and lamina (Fig. 2d), and lenticular phosphate concretions (Figs. 2e, 2f) with thickness ranging from tens of centimetres to 5 meters. At the studied section, the pyritiferous shales grade into the phosphatic shales. Pyrite nodules are usually absent from the phosphatic bed, but some phosphatic concretions are overgrown by a pyritic rim (Fig. 2g). These phosphate concretions are mostly few centimetres in diameter (1-2 cm to 3-7 cm, Fig. 2e-2g), composed of fluorapatite, and occur in high abundance over a short stratigraphic interval of few meters in thickness. Pre-compaction, internal soft-sediment deformation suggests that phosphate concretions formed early on. The overlying Avzyan Formation contains predominantly stromatolitic carbonates with flat-pebble lenses and thin layers of shales and siltstones that probably reflect upward-shallowing, as indicated by multiple exposure surfaces with desiccation cracks in the upper member (Bartley *et al.*, 2007).

We collected two shale samples from the lowermost member of the Satka Formation, 50-55 meters above the altered phosphate-bearing stromatolitic dome near Kusa settlement. Eighteen shale samples were collected from the overlying Bakal Formation, taken from quarries (NovoBakal, Irkuskan, Petlin and Bulandikha) near Bakal City and from one pond bank. The sample set spans the Makar (7 samples), Irkuskan (2 samples), Shuida (7 samples), Bulandikha (2 samples, Table 1) members. The Zigazino-Komarovo Formation was sampled at two quarries (Irkuskan and Petlin) close to Bakal City. We collected eighteen samples, including two below the phosphatic horizon, one phosphate concretion, ten shales from the phosphatic horizon and five shales above phosphorite lenses. Additional five shale samples were taken from the lowermost member of the overlying Avzyan Formation at the Revet River bank. Overall, the 41 shale samples represent a continuous sedimentary sequence from the Satka Formation to the Avzyan Formation (Fig. 1). Nine samples of phosphate nodules were collected from the Zigazino-Komarovo Formation (Petlin Quarry) for direct dating with the Pb-Pb isochron method using a stepwise dissolution technique.

3. Methods

The N and C isotope analytical work followed established protocols and was carried out in the St Andrews Isotope Geochemistry (StAIG) lab at the University of St Andrews (Stüeken *et al.*, 2020). First, each sample was trimmed to remove weathered surfaces. Clean interiors of the rocks were chipped into sub-cm sized pieces and cleaned sequentially in DI-water (18 MΩ cm^{-1}), methanol (reagent grade), 1 M HCl (reagent grade), and more DI-water to remove surface contaminants. The rock chips were swirled with each solvent for about 10 seconds and later dried in a closed oven at 60°C. Once dry, the samples were pulverised in an agate ball mill and then stored in muffled scintillation vials (500°C overnight). The powders were decarbonated with two treatments of 2 M HCl (roughly 10ml per 0.5 g powder) at 60°C. The decarbonated residues were washed three times with DI-water and then dried for three days in a closed oven at 60°C.

The dried powders were weighed into tin capsules (8 x 5 mm, ThermoFisher Scientific) and analysed by flash combustion with an EA IsoLink, coupled via a ConFlo IV to a MAT 253 isotope ratio mass spectrometer (ThermoFisher Scientific). The EA was equipped with a combustion column that was packed with tungstic oxide and electrolytic copper wire, followed by a water trap packed with magnesium perchlorate. This setup allows analyzing carbon, nitrogen and sulphur isotopes (Sayle *et al.*, 2019); however, the sulphur abundances in these samples were mostly below 0.1 wt. %, with few exceptions, which made accurate isotopic measurements challenging. Furthermore, sulphur isotope values for pyrite extracts

have previously been reported (Doyle *et al.*, 2018). The focus of this study is therefore on organic carbon and nitrogen isotopes and their abundances. Isotopic ratios are expressed in standard delta notation: $\delta = (R_{sample}/R_{standard} - 1) \times 1000$, where $R = {}^{13}C/{}^{12}C$ for carbon isotopes (reported as $\delta^{13}C$) and $R = {}^{15}N/{}^{14}N$ for nitrogen isotopes (reported as $\delta^{15}N$). The reference standards are VPDB and atmospheric air, respectively. The analyses were calibrated with USGS-40 and USGS-41. For quality control, we used USGS-20, which was within 0.1 ‰ of accepted value for $\delta^{13}C$ and within 0.3 ‰ for $\delta^{15}N$. The average reproducibility of samples (1 standard deviation) was 0.17 ‰ for $\delta^{13}C$ and 0.35 ‰ for $\delta^{15}N$. Ratios of total organic carbon (TOC) to total nitrogen (TN), abbreviated as C/N, are expressed in units of mol/mol (Table 1).

The U–Pb (or Pb–Pb) method is commonly used to date authigenic apatite of metasomatic (Berger & Braun, 1997; Amelin & Zaitsev, 2002; Barfod *et al.*, 2005) or sedimentary origin (Chen *et al.*, 2004; Ovchinnikova *et al.*, 2008; Kuznetsov *et al.*, 2018). The Pb–Pb isochron age of sedimentary apatite reveals the time of early diagenetic crystallization of phosphate in unconsolidated sediments soon after deposition. However, using microcrystalline apatite as a geochronometer requires application of a chemical stepwise dissolution technique to prevent contamination by Pb derived from detrital silicate and sulfide minerals. The coupled analyses of Pb and Sr isotopic compositions in dissolved fractions reveal contribution of detrital silicate and sulfide minerals to phosphate extracts (Berger & Braun, 1997; Frei *et al.*, 1997; Ovchinnikova *et al.*, 1998; Ovchinnikova *et al.*, 2000; Bolhar *et al.*, 2002; Ovchinnikova *et al.*, 2007; Kuznetsov *et al.*, 2013; Kuznetsov *et al.*, 2017). The method thus allows resolving primary phosphate component for Pb–Pb dating of sedimentary apatite.

The Pb and Sr isotope analyses of phosphorites were performed at IPGG RAS at Saint Petersburg, Russia. The phosphate nodules were cut along the long axis to expose the central part. Before powdering, each chip was washed in ultrapure water in an ultrasonic bath for 10 minutes. The chips were then pulverized and roughly 0.1 g of powder was dissolved sequentially in 0.1 M HCl, 0.5 M HCl and 1 M HCl at room temperature to obtain three fractions named as L1, L2 and L3, respectively (Table 2). The insoluble residues (IR fractions) were dissolved in a mixture of concentrated HF and HNO_3 at 220°C. The column chemistry involved in chemical separation of Pb and Sr for isotope analyses has been described earlier (Ovchinnikova *et al.*, 2000; Ovchinnikova *et al.*, 2012; Kuznetsov *et al.*, 2017). The total blanks of Pb and Sr for the whole procedure were less than 0.1 ng and 4 ng, respectively. The Pb and Sr isotopic composition of each extracted fraction was measured with a Triton TI mass-spectrometer. The average ${}^{87}Sr/{}^{86}Sr$ values for the standards NIST SRM 987 and EN-1 were 0.71027 ± 0.00001 (2σ, n = 24) and 0.70920 ± 0.00002 (2σ, n = 14) during the analytical sessions. Based on repeated analyses of the NBS SRM 982 standard, the measured Pb isotope ratios were corrected for an instrumental fractionation factor of 0.13% per atomic mass unit. Reproducibility of Pb isotope ratios, evaluated with the BCR-1 standard, corresponds to ±0.008% (2σ). The software algorithm of Ludwig (2003) was used to calculate Pb-Pb isochron age (program Isoplot/Ex. Version 1.00).

4. Results

4.1. Sr and Pb isotope ratios and direct dating of phosphorites

We measured Pb and Sr isotopic compositions in 27 fractions produced by stepwise dissolution of nine phosphate nodules. In addition, five silicicate fractions were also analyzed. The Sr content (1770–2040 ppm) in the phosphate nodules of the Zigazino-

Komarovo Formation significantly exceeds the Sr content (280–560 ppm) in the phosphorites of the Satka Formation, which underwent metasomatic recrystallization (Ovchinnikova *et al.*, 2008).

The $^{87}Sr/^{86}Sr$ ratio in most fractions falls within a narrow range (0.7107–0.7128). It increases up to 0.7149 and 0.7168 in the L1 fraction of two samples (Fig. 3). All these $^{87}Sr/^{86}Sr$ ratios are much higher than were in the contemporaneous Mesoproterozoic seawater (0.7048–0.7058; (Kuznetsov *et al.*, 2014), which indicates that the phosphate nodules did not form in equilibrium with seawater. Instead, apatite growth took place within unconsolidated sediments.

The $^{206}Pb/^{204}Pb$ ratios for the L1 (35.850–55.354), L2 (37.184–65.547) and L3 (35.938–47.695) fractions all show a similar range (Table 2). In contrast, the $^{206}Pb/^{204}Pb$ ratio for the IR fraction (23.243–29.502) is lower than that for most phosphate fractions (Fig. 4). The L1 fraction with the highest $^{87}Sr/^{86}Sr$ ratio of 0.7168 corresponds to low radiogenic Pb ratio ($^{206}Pb/^{204}Pb$ = 27.110) of the corresponding non-phosphate residue (Fig. 4). The other L1 fraction with high $^{87}Sr/^{86}Sr$ (0.7149) corresponds to an abnormally radiogenic Pb isotope composition. The data suggest that these two L1 fractions are contaminated with Pb derived from sulfide, silicate and TR-rich minerals, respectively. These two data-points for the contaminated L1 fractions are omitted from age calculations. In a $^{207}Pb/^{204}Pb$–$^{206}Pb/^{204}Pb$ diagram, the remaining 25 data-points for all three fractions form a well-fitted line (Fig. 4), which corresponds to a Pb–Pb isochron date of 1330 ± 20 Ma (MSWD = 3.7). The obtained date is interpreted as the early diagenetic crystallization age of phosphate nodules formed soon after deposition of the Zigazino-Komarovo Formation shales.

4.2. Nitrogen and organic carbon content and isotope ratios

The black shales of the Burzyan and Yurmatau groups show distinct distribution in organic carbon and nitrogen abundances and nitrogen and organic carbon isotope ratios with internal variability (Table 1). In the black shales of the Burzyan Group and in the Avzyan Formation of the Yurmatau Group, TOC abundance in decarbonated residues is mostly lower by a factor of about 5 than in the Zigazino-Komarovo Formation. In contrast, their TN content is similar or higher, such that the Burzyan Group and the Avzyan Formation display much lower C/N ratios (mostly < 10) than the Zigazino-Komarovo Formation (mostly > 50). In both units, TOC and TN contents are correlated with each other (Fig. 3) with correlation coefficients (R^2) of 0.4 and 0.7, respectively.

Within the Burzyan Group, both TOC and TN contents decrease upsection through the Bakal Formation by factors of about 2 and 5, respectively (Fig. 4). These trends track the transition from black shales to stromatolites. Nitrogen isotope values in black shales of the lower Bakal Formation cluster around a mean of +2.7 ± 0.2 ‰ (1SD, n = 7) and increase to a mean of +4.9 ± 0.3 ‰ (n = 7) in the upper stromatolitic part. Organic carbon isotope values in black shales decrease slightly across the same interval from -28.5 ± 0.3 ‰ in the lower part to -29.6 ± 0.7 ‰ in the stromatolite-bearing part.

In the Yurmatau Group, nitrogen isotopes in black shales are highest in the phosphorite-rich interval of the Zigazino-Komarovo Formation with a mean of +7.2 ± 0.3 ‰ (n = 9; Fig. 4). Two subsamples of diagenetic phosphate nodule have values of +5.2 ‰ and +6.7 ‰. Shales from a few meters below the phosphatic horizon have a mean of +4.9 ± 0.3 ‰ (n = 4), and those immediately above it fall around +5.8 ± 1.3 ‰ (n = 4). Organic carbon isotope values in black shales tend to be slightly more positive within the phosphatic horizon (-27.3 ± 0.3 ‰, n = 9) and immediately above it (-27.1 ± 1.4 ‰, n = 4) than in the underlying non-phosphatic shales (-29.1 ± 1.7 ‰, n = 4). The reported average $\delta^{13}C_{org}$ value for black shales of the uppermost member of the Zigazino-Komarovo Formation, which was not sampled in this study, is -25.8 ± 0.4 ‰ (Bartley *et al.*, 2007), and slightly higher than what

we obtained for the lower and middle members. The diagenetic phosphate nodule shows a relatively high $\delta^{13}C_{org}$ value of -22.9 ‰. We emphasize that samples from the same member taken from different sections agree in their geochemical results, which suggests an absence of strong secondary alteration of the sampled horizons.

Five samples of black shale from the overlying stromatolite member of the Avzyan Formation show the mean $\delta^{15}N$ value of +4.6 ± 1.4 ‰ and the average $\delta^{13}C$ value of -26.1 ± 1.1 ‰. The latter value is much lower than the average value of $\delta^{13}C_{org}$ (-22.2 ± 1.7 ‰) reported for the Avzyan Formation shales in the eastern, more altered section (Bartley *et al.*, 2007).

5. Discussion

5.1. Post-depositional alteration of primary signals

The Riphean strata in the western margin of the South Urals are essentially unmetamorphosed (Maslov *et al.*, 2001; Glasmacher *et al.*, 2004), such that metamorphism has probably not had a measurable impact on primary N and C isotopic signatures in organic-rich shales. Carbon and nitrogen isotopes undergo significant shift of more than 1 ‰ only at greenschist facies and above (Schidlowski, 2001; Thomazo & Papineau, 2013). Furthermore, previous studies of the carbonate intervals found the average $\delta^{13}C_{carb}$ and $\delta^{18}O_{carb}$ values of -0.6 ± 0.5 ‰ and -8.8 ± 2.2 ‰, respectively, for the Burzyan Group (Semikhatov *et al.*, 2009), and 1.2 ± 1.1 ‰ and -7.2 ± 3.4 ‰, respectively, for the Avzyan Formation of the Yurmatau Group (Bartley *et al.*, 2007), which are close to the typical values for the Mesoproterozoic marine carbonates. These findings suggest insignificant thermal alteration and meteoric diagenesis.

However, some degree of post-depositional diagenesis of organic carbon and nitrogen is unavoidable. Under anoxic diagenetic conditions, which likely dominated throughout the deposition of Burzyan and Yurmatau group shales, as indicated by iron speciation (Doyle *et al.*, 2018), the three main diagenetic pathways (Lehman *et al.*, 2002) to consider are (a) preferential degradation of labile molecules, such as proteins and carbohydrates, compared to more refractory lipids (decreasing residual $\delta^{13}C$ and $\delta^{15}N$ values by a few permil); (b) kinetic fractionation during hydrolysis of labile compounds (increasing residual $\delta^{13}C$ and $\delta^{15}N$ values by a few permil); and (c) addition to biomass from benthic organisms (isotopic effects dependent on the type of metabolism). Pathway (a) and (b) occur in tandem and are therefore not expected to result a significant net isotopic effect on residual biomass (Lehman *et al.*, 2002). The organic matter extracted from the phosphate nodule in this study can provide insights into the magnitude and direction of diagenetic alteration, if this phosphate-bound material represents the diagenetically unaffected component. Within the phosphate nodule, δ^{13}Corg value is ~4.4 ‰ higher and $\delta^{15}N$ value is ~2 ‰ lower than in the surrounding shales, suggesting that the residual refractory biomass in the shales is slightly depleted in ^{13}C and enriched in ^{15}N compared to its initial composition. However, empirical observations from modern anoxic environments and/or depositing settings with sedimentation rate suggest that the overall effect on residual biomass is minor (< 1-2 ‰ for both $\delta^{13}C$ and $\delta^{15}N$ values; (McArthur *et al.*, 1992; Robinson *et al.*, 2012). Furthermore, the effects would likely have been similar across the sedimentary package, meaning that relative changes are likely to be preserved.

In case of nitrogen, an important side-effect of anoxic biomass degradation is the release of ammonium into pore waters. Unlike organic carbon oxidation to CO_2 by anaerobic metabolisms, such as sulphate or iron reduction, ammonium oxidation is thermodynamically unfavourable in the absence of oxygen (Stüeken *et al.*, 2016). It can therefore build up in pore

waters to millimolar concentrations (Rosenfeld, 1979; Boudreau & Canfield, 1988). Some of this diagenetic ammonium gets incorporated into clay minerals, in substitution for potassium (Schroeder & McLain, 1998), leading to a decrease in the bulk sedimentary organic C/N ratio (Müller, 1977; Freudenthal *et al.*, 2001; Chen *et al.*, 2019). It is likely that some of this ammonium would also diffuse into adjacent sedimentary beds or into the overlying anoxic water column. However, this low-temperature diffusion process does not impart any isotopic fractionation (Koehler *et al.*, 2019). In our sample set, it is noteworthy that the phosphoritic Zigazino-Komarovo Formation displays consistently higher C/N ratios than the other units that are devoid of phosphate enrichment. As further discussed below, this difference may reflect a higher degree of aerobic respiration and ammonium oxidation (nitrification) during deposition of the Zigazino-Komarovo Formation, such that less ammonium built up in the water column and in clay minerals.

5.2. Redox stratification in the Lower Riphean

In the Burzyan Group, which was likely deposited in a partially restricted marine basin (Maslov *et al.*, 1997), $\delta^{15}N$ values increase with decreasing water depth from the shale-dominated beds to the stromatolitic beds. The lowest N isotope values occur in the black shales of the lowermost member of the Bakal Formation, whereas the highest values are found in the stromatolitic carbonate facies of the upper Bakal Formation. This facies trend has previously been interpreted as progressive shoaling (Semikhatov *et al.*, 2009). A similar basinal gradient in nitrogen isotope values has been documented from the Mesoproterozoic (~1.45 Ga) Belt Supergroup in USA (Stüeken, 2013), and from the ~1.65 Ga Bangemall Supergroup and ~1.4 Ga Roper Group in Australia (Koehler *et al.*, 2017; Cox *et al.*, 2019). Offshore marine facies of the ~1.2 Ga Vindhyan Basin in India are also isotopically light ($\delta^{15}N < +3$ ‰; (Gilleaudeau *et al.*, 2020), while more positive nitrogen isotope values (> +4 ‰) have been reported from shallow-water sedimentary rocks of the ~1.56 Ga Gaoyuzhuang Formation in the Jixian Group of China (Wang *et al.*, 2020b). Combined with our data for the Bakal Formation, these observations suggest redox stratification in the marine nitrogen cycle within several Mesoproterozoic basins. Consistent with this interpretation, Doyle *et al.* (2018) found evidence of pervasively ferruginous conditions in the water column below a thin oxic surface layer based on iron speciation and trace element analyses of the Riphean strata.

Marine nitrogen is sourced from biological N_2 fixation, which produces ammonium (NH_4^+) with an isotopic composition around -1 ‰ (Zhang *et al.*, 2014). Ammonium can be directly utilized as a nutrient under anoxic conditions, in particular by bacteria, which outcompete eukaryotes in ammonium uptake (Karl *et al.*, 2001; Bouman *et al.*, 2011; Fawcett *et al.*, 2011). Partial ammonium assimilation favours ^{14}N over ^{15}N with a fractionation of 14 to 27 ‰, rendering biomass isotopically light and residual ammonium heavy (Hoch *et al.*, 1992). However, very negative $\delta^{15}N$ values in ancient biomass that resulted from partial ammonium assimilation are very rare in the geologic record (Stüeken *et al.*, 2016), suggesting that assimilation went to completion without net isotopic effects. Such complete ammonium assimilation is observed in modern microbial cultures when dissolved ammonium concentrations are in the range of 10 μM or less (Hoch *et al.*, 1992). If these data from modern cultures are relevant to the Precambrian, they suggest that the anoxic deep ocean did not have a large ammonium reservoir at this time. This inference is consistent with the high energetic cost of biological N_2 fixation (Shanmugam *et al.*, 1978): if dissolved ammonium had built up to high concentrations, N_2 fixation would likely have ceased until the available ammonium was nearly fully consumed. Hence sedimentary $\delta^{15}N$ values close to zero permil are most parsimoniously explained by an anaerobic N cycle, dominated by production and recycling of ammonium with an overall small ammonium reservoir.

In the presence of nanomolar levels of O_2, ammonium is rapidly oxidized (nitrified) to nitrate (NO_3^-; (Lipschultz *et al.*, 1990; Bristow *et al.*, 2016). Under oxic conditions, as in the modern ocean, nitrate is therefore the major form of dissolved N, and it is readily bioavailable to eukaryotic algae (Glass *et al.*, 2009). Under suboxic conditions, such as in modern oxygen-minimum zones and in sedimentary pore waters, nitrate is reduced to either ammonium (dissimilatory nitrate reduction to ammonium) or N_2 gas (denitrification), and this process imparts a negative isotopic fractionation of 10-15 ‰ on reduction products (Kritee *et al.*, 2012). Modern marine nitrate, as well the biomass of nitrate-assimilating organisms, are therefore isotopically enriched to about +5 ‰. In a redox-stratified setting, nitrification likely occurs in the oxic photic zone, similar to today where 80-90 % of biomass remineralization takes place in the top 200 meters of the water column (Martin *et al.*, 1987; Emerson & Hedges, 1988). However, the isotopic signature of biological nitrate assimilation can only be expressed in marine sediments, if the nitrate reservoir is large enough, such that nitrate-assimilating organisms make up a significant fraction of the buried biomass (Kipp *et al.*, 2018). The data from the upper Bakal Formation and other Mesoproterozoic basins discussed above indicate that this was the case in shallow-marine settings at this time. Oxygenic photosynthesizers within the stromatolitic microbial communities may have contributed to strongly oxic conditions and rapid nitrate production in surface waters. In contrast, deeper marine settings, as captured by the thick black shales of the lower Bakal Formation, were likely characterized by low concentrations of ammonium. Organic carbon isotope values, which are slightly more negative in the stromatolitic facies, may indicate secondary, anaerobic carbon cycling within microbial mats, as was observed in the Mesoproterozoic Belt Supergroup of USA (Stüeken, 2013). Overall, the Lower Riphean strata of the Burzyan Group thus capture redox stratification in the marine nitrogen cycle under restricted basinal conditions where coastal upwelling was absent.

5.3. Phosphogenesis and transient ocean oxygenation in the Middle Riphean

The phosphoritic interval in the Middle Riphean Zigazino-Komarovo Formation appears to mark a significant deviation from this pattern. Such high abundances of phosphate nodules, as observed in this unit (Fig. 2e-2g), are unknown for the Mesoproterozoic (Papineau, 2010). Similar to modern phosphorite deposits, and consistent with the less restricted marine setting of the Bashkir Basin during the Middle Riphean, this phosphoritic interval is most parsimoniously explained by coastal upwelling of phosphate-rich waters. The fertilization effect of coastal upwelling can extend well into the interior of epeiric seas (Pufahl & Groat, 2017) and is therefore not inconsistent with a relatively shallow-marine depositional setting above the fairweather wave-base. This interpretation is also supported by the abundance of pyrite nodules immediately beneath the phosphatic horizon (Ovchinnikova *et al.*, 2013) and by the high abundance of organic carbon, similar to modern upwelling zones (Premuzic *et al.*, 1982; Brüchert *et al.*, 2003). Today, sediments from upwelling zones show some of the highest $\delta^{15}N$ values up to about +10 ‰ (Tesdal *et al.*, 2013); not too dissimilar from the relatively high values of up to +7.6 ‰ in the Zigazino-Komarovo Formation.

In the modern ocean, these high nitrogen isotope values are produced by an advanced degree of denitrification in the water column in high-productivity upwelling zones (Sigman *et al.*, 2009). However, they can only be preserved in sediments because the modern marine nitrate reservoir of the deep ocean is large, such that it does not become fully depleted, even at these high denitrification rates (Kipp *et al.*, 2018). If Mesoproterozoic deep waters were anoxic, they should have been devoid of nitrate, as well as phosphate, which is rapidly removed under ferruginous conditions (Reinhard *et al.*, 2017). The accumulation of phosphorite and the preservation of evidence for a nitrate reservoir in this highly productive,

shallow-marine upwelling zone of the Bashkir Basin are thus best explained by upwelling of deep-marine waters that were suboxic or oxic in composition. This interpretation is also consistent with the relatively high C/N ratios in these rocks in comparison to the Lower Riphean strata deposited in a more restricted setting, because a higher degree of aerobic respiration would have further depleted the ammonium reservoir of deep waters.

It is important to point out that the entrainment of oxygen into deep-marine waters could have been a purely regional and temporally restricted phenomenon within this basin. In fact, moderately low molybdenum and uranium abundances in black shales of the Zigazino-Komarovo Formation (Doyle *et al.*, 2018) suggest that the global ocean might not have been oxic at this time, at least over geochemically relevant period to the residence time of these elements, which is also supported by the relatively short stratigraphic extent of this phosphatic interval. However, our interpretation adds to previous evidence for at least locally and transiently suboxic deep waters in the mid-Proterozoic (Slack *et al.*, 2007; Slack *et al.*, 2009; Sperling *et al.*, 2014; Planavsky *et al.*, 2018; Wang *et al.*, 2020a) and suggests that upwelling of oxic water masses may have locally stimulated biological productivity and maintained restricted refugees that could have been inhabited by eukaryotic life (cf. Johnston et al., 2012).

6. Conclusion

The redox state of the Proterozoic ocean is a widely debated topic, because it has profound implications for our understanding of what constrained the early evolution of complex organisms (Lenton *et al.*, 2014; Planavsky *et al.*, 2014; Butterfield, 2018). The conventional view has evolved from the one of widespread oxygenation following the early Paleopoterozoic Great Oxidation Event (Holland, 1984) to the one of extensive euxinia (Canfield, 1998; Poulton *et al.*, 2004) and subsequently to the one inferring predominantly ferruginous deep-marine conditions (Planavsky *et al.*, 2011; Poulton & Canfield, 2011; Sperling *et al.*, 2015), capped by an oxic surface layer (Hardisty *et al.*, 2017) and locally developed (in oxygen-minimum zones and epicontinental basins) euxinic margins (Poulton *et al.*, 2010; Gilleaudeau & Kah, 2015; Wang *et al.*, 2020a). Our data from the Lower Riphean Burzyan Group support this latter view, because evidence for replete dissolved nitrate is limited to shallow-marine facies, while deeper-marine settings were apparently characterized by low levels of ammonium and absence of nitrate.

However, it seems unlikely that the mid-Proterozoic ocean was spatially and temporally redox-homogeneous for over a billion years, given that even in the modern ocean significant heterogeneity exists despite ocean circulation and during climatic perturbations that cause heterogeneity in productivity and entrainment of oxygen into colder waters. Several recent studies have documented redox heterogeneity in the mid-Proterozoic, including evidence for suboxic to oxic bottom waters (Slack *et al.*, 2007; Slack *et al.*, 2009; Sperling *et al.*, 2014; Planavsky *et al.*, 2018; Wang *et al.*, 2020a). We propose that the accumulation of phosphate in the Middle Riphean Zigazino-Komarovo Formation, paired with high nitrogen isotope values, and high TOC content and C/N ratios, are best explained by upwelling of oxic waters that were enriched in phosphate and nitrate, locally stimulating biological productivity. A Pb-Pb isochron based on nine phosphate nodules of the Zigazino-Komarovo Formation provides a direct age constraint of 1330 ± 20 Ma for this Mesoproterozoic phosphogenesis event in the South Urals. This deep-marine oxygenation episode was perhaps short-lived and regional in extent, but it may nevertheless represent a pattern in deep-marine ocean circulation that maintained locally significant oxygenated habitats where eukaryotic life could linger until the Neoproterozoic expansion into the marine realm.

Acknowledgements

EES acknowledges start-up funds from the School of Earth & Environmental Sciences at the University of St Andrews. The isotope work was supported by RFBR project 19-05-00623. This contribution is dedicated to Galina Ovchinnikova, a pioneer in U-Pb dating of sedimentary apatite at IPGG RAS (St. Petersburg, Russia).

Figures

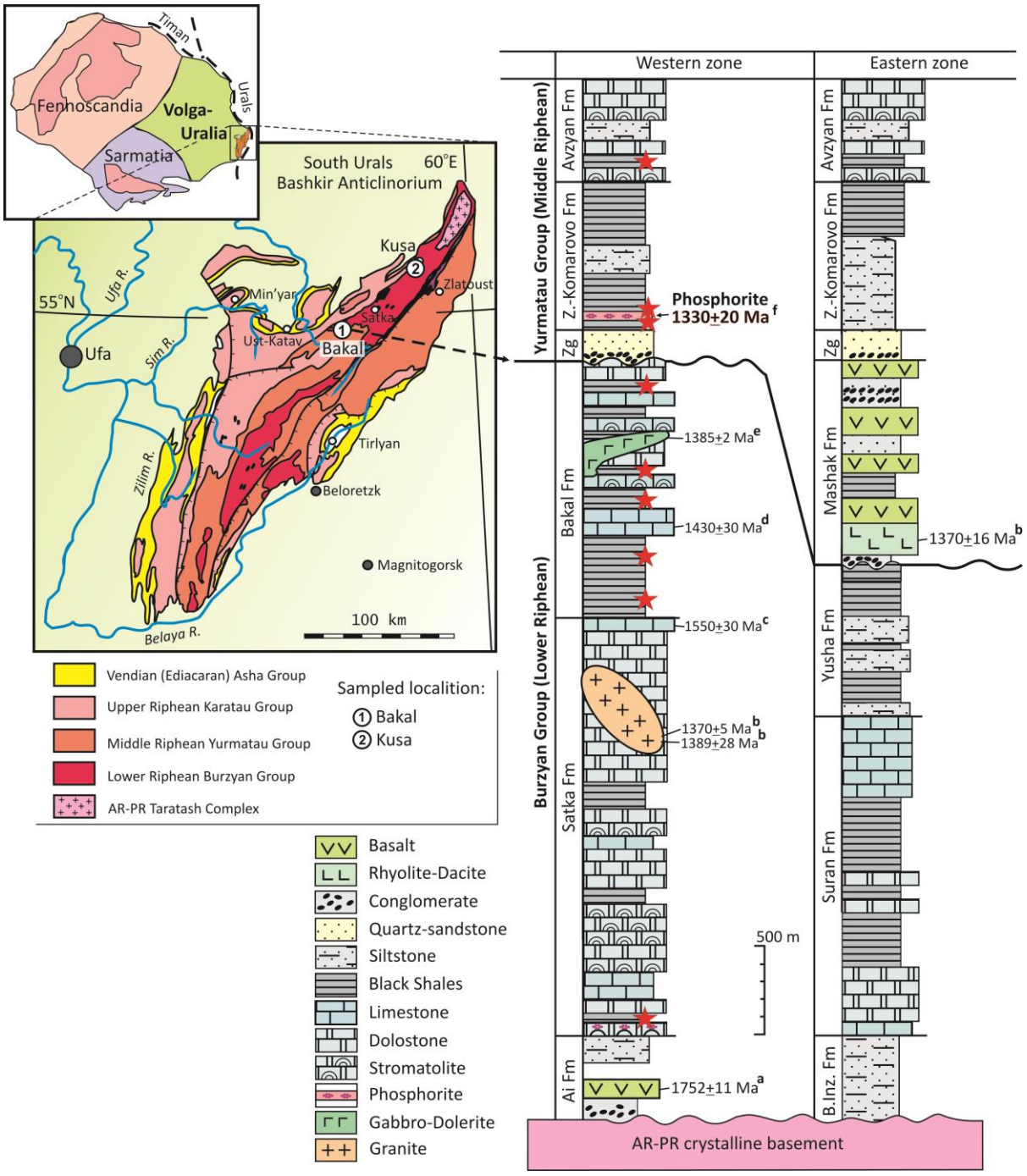

Figure 1: Geological map with sampled localities (left) and stratigraphy of the Riphean strata in the South Ural Mountains (right). Horizons analyzed in this study are highlighted with red stars. Age constrains: a - Krasnobayev et al., 2013; Puchkov et al., 2014; b - Ronkin et al. (2007); c - Kuznetsov et al. (2008); d – Kuznetsov et al. (2013); e - Ernst et al. (2006); f - this study. Zg stands fort he Zilgalga Formation, Z.-Komarovo Fm. for the Zigazino-Komarovo Formation and B.Inz. Formation for the Bolshoi Inzer Formation.

Figure 2: Field pictures of the studied intervals. (a) Stromatolitic dome with phosphate cement from the Satka Formation with cross-cutting quartz veins. (b) Deep-water shales from the Lower Bakal Formation. (c) Shales interbedded with stromatolitic bioherms in the Upper Bakal Formation. (d) Diagenetic pyrite lamina in the lower part of the Zigazino-Komarovo Formation. (e-f) Phosphate concretion horizon in the Zigazino-Komarovo Formation (e = plan view, f = side view). (g) Zoned concretion with a phosphate core and a pyrite rim. (h) Wave-rippled sandstones above the phosphatic horizon of the Zigazino-Komarovo Formation.

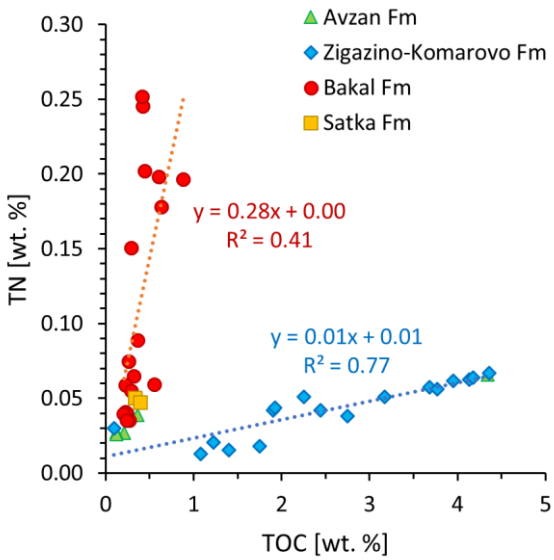

Figure 3: Scatter graph of total nitrogen versus total organic carbon, illustrating higher C/N ratios of the Zigazino-Komarovo Formation compared to all other units. Not shown are data for the phosphate nodule with 31.27 wt. % TOC and 0.34 wt. % TN from the Zigazino-Komarovo Formation. The latter data also plot along the trendline for the Zigazino-Komarovo Formation.

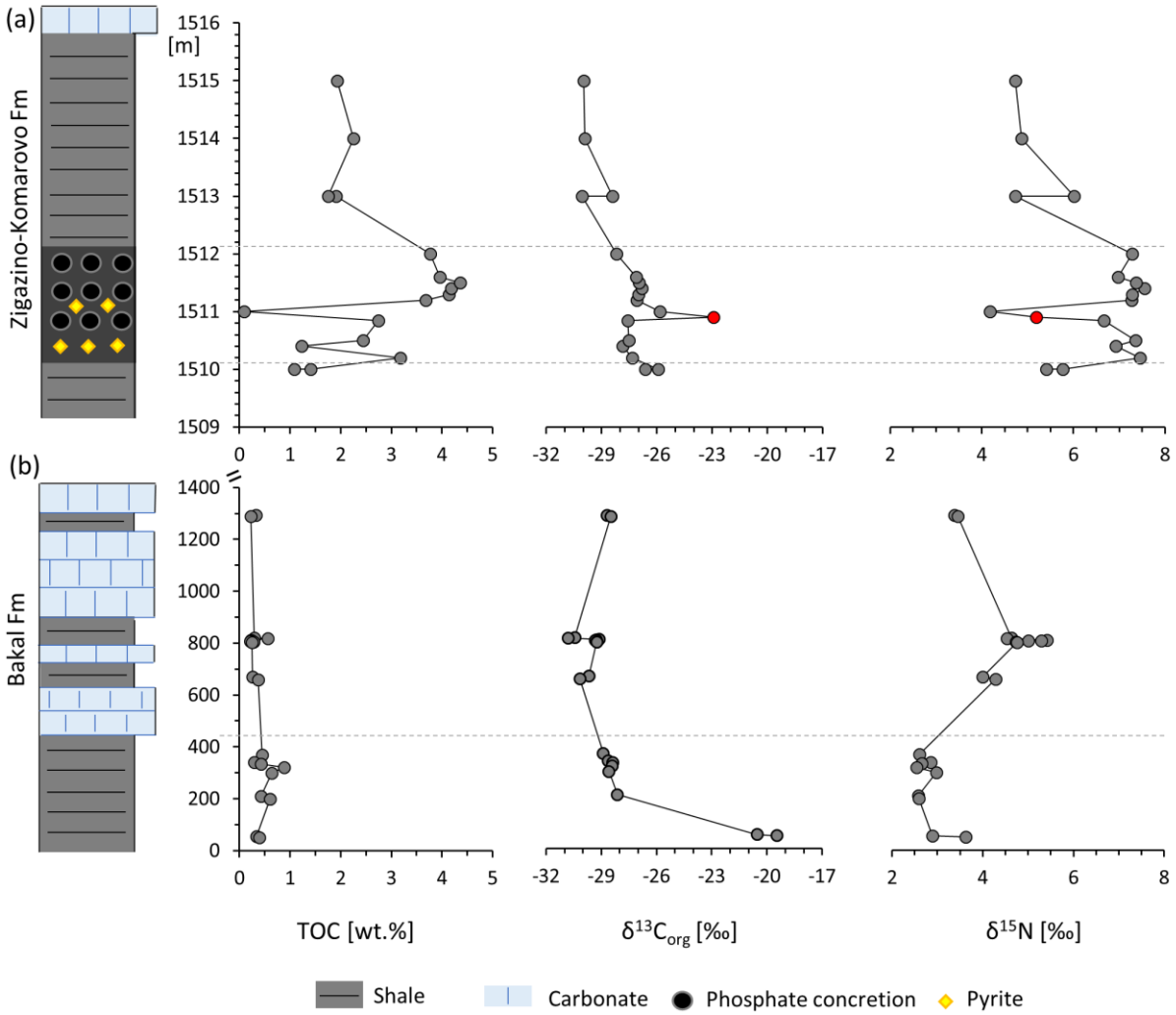

Figure 4: Stratigraphy of the analysed sections in the Zigazino-Komarovo Formation (a) and the Bakal Formation (b). In panel (a) the red data-point marks the phosphate nodule. It is not shown on the TOC graph. Horizontal dashed lines mark the stratigraphic position of the phosphorite member in (a) and the transition from the Lower to the Upper Bakal Formation in (b).

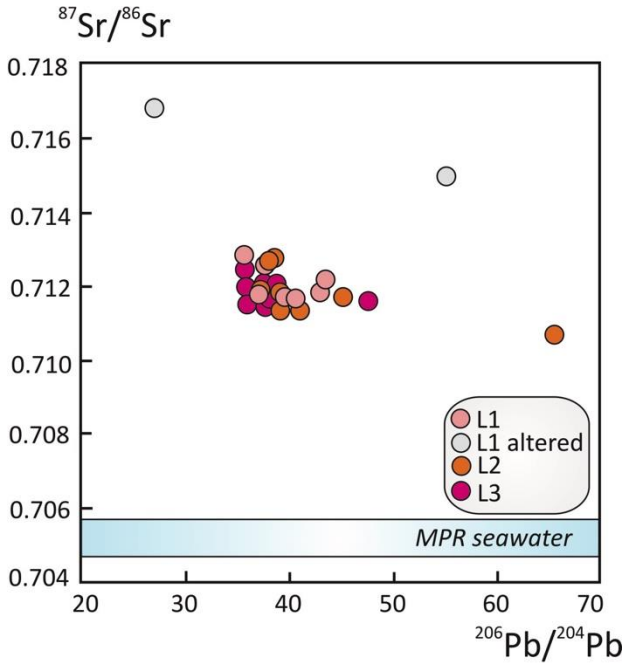

Figure 5: Scatter graph of $^{87}Sr/^{86}Sr$ versus $^{206}Pb/^{204}Pb$ ratios for fractions obtained by stepwise dissolution of phosphate nodules of the Zigazino-Komarovo Formation in 0.1, 0.5 and 1 N HCl. The $^{87}Sr/^{86}Sr$ ratio in phosphate nodules is higher than in contemporaneous Mesoproterozoic seawater (Kuznetsov *et al.*, 2014). The two L1 fractions are contaminated by trace elements derived from siliciclastic materials.

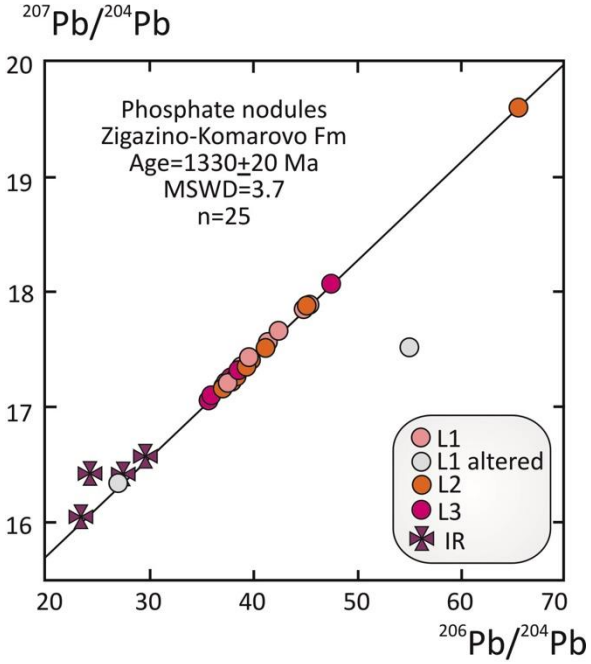

Figure 6: $^{207}Pb/^{204}Pb$ and $^{206}Pb/^{204}Pb$ ratios for phosphate nodules of the Zigazino-Komarovo Formation; L1, L2 and L3 fractions were obtained by stepwise dissolution in 0.1, 0.5 and 1 N HCl, respectively; IR – insoluble residue in 1 N HCl. The Pb isotopic ratios (except for the two altered L1 fractions) define a straight line, which corresponds to an age 1330 ± 20 Ma (MSWD = 3.7, n = 25).

Tables

Table 1: Organic carbon and total nitrogen data for decarbonated residues. Sample UZF15-1_N is a phosphate nodule.

Sample ID		Position [m]	TOC [%]	$\delta^{13}C$ [‰]	TN [%]	$\delta^{15}N$ [‰]	C/N [at]	Locality
Yurmatau Group:								
Avzyan Formation:								
U16-109		2440	0.36	-24.87	0.04	4.53	11.0	Revet
U16-101		2414	4.34	-27.92	0.07	7.13	76.8	Revet
U16-100		2413	0.21	-25.49	0.03	3.66	9.1	Revet
U16-99		2412	0.12	-26.12	0.03	3.74	5.2	Revet
U16-97		2410	0.12	-25.87	0.03	4.00	5.5	Revet
Zigazino-Komarovo Formation:								
U16-26		1510.0	1.08	-26.63	0.01	5.41	99.2	Irkuskan
U16-48		1510.0	1.40	-25.92	0.02	5.77	106.8	Petlin
UZ15-9		1510.2	3.17	-27.34	0.05	7.46	72.4	Petlin
UZ15-8		1510.4	1.23	-27.85	0.02	6.93	69.3	Petlin
UZ15-7		1510.5	2.44	-27.51	0.04	7.36	67.6	Petlin
UZF15-1		1510.9	2.75	-27.57	0.04	6.67	84.4	Petlin
UZF15-1_N		1510.9	31.27	-22.91	0.34	5.20	108.1	Petlin
U16-50		1511.0	0.10	-25.83	0.03	4.18	3.7	Petlin
UZ15-1		1511.2	3.68	-27.09	0.06	7.26	74.6	Petlin
UZ15-2		1511.3	4.14	-26.99	0.06	7.28	77.3	Petlin
UZ15-3		1511.4	4.18	-26.83	0.06	7.55	76.4	Petlin
UZ15-4		1511.5	4.36	-26.96	0.07	7.37	76.1	Petlin
UZ15-5		1511.6	3.95	-27.12	0.06	6.97	74.8	Petlin
U16-49		1512.0	3.77	-28.18	0.06	7.28	78.2	Petlin
U16-27		1513.0	1.90	-30.07	0.04	4.73	52.8	Irkuskan
U16-51		1513.0	1.75	-28.42	0.02	6.02	113.1	Petlin
U16-28		1514.0	2.26	-29.91	0.05	4.87	51.7	Irkuskan
U16-29		1515.0	1.93	-29.99	0.04	4.73	51.7	Irkuskan
Burzyan Group:								
Bakal Formation:	*Member:*							
U16-31	Bulandikha	1294	0.32	-28.69	0.06	3.37	5.8	Budlandikha
U16-30	Bulandikha	1290	0.23	-28.48	0.06	3.45	4.5	Budlandikha
U16-47	Shuida	820	0.29	-30.45	0.05	4.63	6.3	Petlin
U16-45	Shuida	818	0.55	-30.80	0.06	4.53	11.0	Petlin
U16-25	Shuida	812	0.23	-29.12	0.04	5.42	6.4	Irkuskan
U16-24	Shuida	810	0.24	-29.26	0.04	5.29	7.1	Irkuskan
U16-23	Shuida	808	0.21	-29.32	0.04	5.01	6.2	Irkuskan
U16-22	Shuida	805	0.27	-29.23	0.04	4.74	9.1	Irkuskan
U16-21	Shuida	802	0.25	-29.24	0.03	4.75	8.2	Irkuskan
U16-44	Irkuskan	670	0.26	-29.68	0.07	4.00	4.1	Petlin
U16-43	Irkuskan	660	0.36	-30.16	0.09	4.28	4.8	Petlin

U16-38	Makar	370	0.45	-28.89	0.20	2.60	2.6	Novobakal
U16-37	Makar	340	0.30	-28.64	0.15	2.85	2.3	Novobakal
U16-36	Makar	335	0.43	-28.37	0.25	2.65	2.0	Novobakal
U16-35	Makar	320	0.88	-28.42	0.20	2.55	5.2	Novobakal
U16-34	Makar	300	0.64	-28.60	0.18	2.97	4.2	Novobakal
U16-53	Makar	210	0.42	-28.12	0.25	2.58	2.0	Pond
U16-52	Makar	200	0.61		0.20	2.59	3.6	Pond
Satka Fm:								
U16-112	Kusa	55	0.34	-20.54	0.05	2.89	7.8	Kusa
U16-111	Kusa	50	0.39	-19.47	0.05	3.63	9.6	Kusa

Table 2: Pb and Sr isotope composition of leach fractions of phosphate nodules from the Zigazino-Komarovo Formation.

Sample	Fraction [a,b]	Weight of fraction, %	$^{206}Pb/^{204}Pb^{c}$	$^{207}Pb/^{204}Pb^{c}$	$^{208}Pb/^{204}Pb$	$^{87}Sr/^{86}Sr$
ZKP-1	*L1*	12	*27.110*	*16.355*	41.771	0.71676
	L2	26	39.696	17.411	46.460	0.71159
	L3	42	37.916	17.249	41.861	0.71153
	IR	19	27.386	16.416	39.639	-
ZKP-4	L1	18	40.694	17.492	44.703	0.71163
	L2	24	37.184	17.171	39.040	0.71187
	L3	23	37.199	17.174	38.759	0.71179
	IR	34	24.116	16.425	36.888	-
ZKP-6	L1	22	37.769	17.242	39.373	0.71254
	L2	21	38.457	17.271	38.814	0.71271
	L3	29	38.809	17.333	41.513	0.71188
	IR	28	29.498	16.573	38.978	-
ZKP-11	L1	16	35.850	17.051	38.932	0.71282
	L2	20	38.014	17.226	38.721	0.71261
	L3	33	36.030	17.069	38.668	0.71199
	IR	25	23.243	16.052	37.862	-
ZKP-12	L1	19	37.261	17.186	51.793	0.71174
	L2	23	39.326	17.361	51.033	0.71132
	L3	42	35.938	17.071	41.592	0.71250
ZKP-14	L1	17	39.821	17.404	54.351	0.71162
	L2	40	41.162	17.520	52.975	0.71130
	L3	22	37.600	17.220	43.882	0.71200
	IR	18	29.502	16.569	40.200	-
ZKP-15	*L1*	20	*55.354*	*17.548*	48.836	0.71491
	L2	21	65.547	19.609	57.418	0.71065
	L3	50	47.695	18.072	46.900	0.71156
ZKP-16	L1	14	43.618	17.706	44.371	0.71211
	L2	32	39.387	17.361	42.672	0.71175
	L3	48	36.057	17.089	41.262	0.71152
ZKP-17	L1	14	43.114	17.681	47.906	0.71177
	L2	24	45.340	17.888	49.269	0.71165
	L3	48	37.917	17.271	42.853	0.71147

[a] Fraction L1 was obtained by dissolution of phosphorite sample in 0.1 N HCl, sequential fraction L2 in 0.5 N HCl and fraction L3 in 1 N HCl. IR is siliciclastic and pyrite residue insoluble in 1 N HCl.
[b] Data for the altered ("secondary") phosphate material are shown in italics and were not used in calculation. 2σ [%] for $^{206}Pb/^{204}Pb$ = 0.07, $^{207}Pb/^{204}Pb$ = 0.09 and $^{208}Pb/^{204}Pb$ = 0.12.

References

Amelin Y, Zaitsev AN (2002) Precise geochronology of phosphorites and carbonatites: the critical role of U-series disequilibrium in age interpretations. *Geochimica et Cosochimica Acta,* **66**, 2399-2419.

Anbar AD, Knoll AH (2002) Proterozoic ocean chemistry and evolution: a bioinorganic bridge? *Science*, **297**, 1137-1142.

Barfod GH, Krogstad EJ, Frei R, Albarede F (2005) Lu-Hf and PbSL geochronology of apatites from Proterozoic terranes: A first look at Lu-Hf isotopic closure in metamorphic apatite. *Geochimica et Cosochimica Acta*, **60**, 1847-1859.

Bartley JK, Kah LC, McWilliams JL, Stagner AF (2007) Carbon isotope chemostratigraphy of the Middle Riphean type section (Avzyan Formation, Southern Urals, Russia): signal recovery in a fold-and-thrust belt. *Chemical Geology*, **237**, 211-232.

Berger M, Braun I (1997) Pb-Pb dating of apatite by a stepwise dissolution technique. *Chemical Geology*, **142**, 23-40.

Bolhar R, Hofmann A, Woodhead J, Hergt J, Dirks P (2002) Pb- and Nd-isotope systematics of stromatolitic limestones from the 2.7 Ga Ngezi Group of the Belingwe greenstone belt: constraints on timing of deposition and provenance. *Precambrian Research,* **114**, 277-294.

Boudreau BP, Canfield DE (1988) A provisional diagenetic model for pH in anoxic porewaters: Application to the FOAM site. *Journal of Marine Research,* **46**, 429-455.

Bouman HA, Ulloa O, Barlow R, Li WK, Platt T, Zwirglmaier K, Scanlan DJ, Sathyendranath S (2011) Water-column stratification governs the community structure of subtropical marine picophytoplankton. *Environmental Microbiology Reports*, **3**, 473-482.

Bristow LA, Dalsgaard T, Tiano L, Mills DB, Bertagnolli AD, Wright JJ, Hallam SJ, Ulloa O, Canfield DE, Revsbech NP, Thamdrup B (2016) Ammonium and nitrite oxidation at nanomolar oxygen concentrations in oxygen minimum zone waters. *Proceedings of the National Academy of Sciences*, **113**, 10601-10606.

Brüchert V, Jørgensen BB, Neumann K, Riechmann D, Schlösser M, Schulz H (2003) Regulation of bacterial sulfate reduction and hydrogen sulfide fluxes in the central Namibian coastal upwelling zone. *Geochimica et Cosmochimica Acta,* **67**, 4505-4518.

Butterfield NJ (2018) Oxygen, animals and aquatic bioturbation: An updated account. *Geobiology*, **16**, 3-16.

Canfield DE (1998) A new model for Proterozoic ocean chemistry. *Nature,* **396**, 450-453.

Chaudhuri R (1980) Stromatlitic Phosphorite in Jhamarcotra. *Geological Survey of India,* **44**, 330-339.

Chen DF, Dong WQ, Zhu BQ, Chen XP (2004) Pb-Pb ages of Neoproterozoic Douchantuo phosphorites in South China: constraints on early metazoan evolution and glaciation events. *Precambrian Research*, **132**, 123-132.

Chen Y, Diamond CW, Stüeken EE, Cai C, Gill BC, Zhang F, Bates SM, Chu X, Ding Y, Lyons TW (2019) Coupled evolution of nitrogen cycling and redoxcline dynamics on the Yangtze Block across the Ediacaran-Cambrian transition. *Geochimica et Cosmochimica Acta,* **257**, 243-265.

Cook PJ (1992) Phosphogenesis around the Proterozoic–Phanerozoic transition. *Journal of the Geological Society,* **149**, 615-620.

Cox GM, Sansjofre P, Blades ML, Farkas J, Collins AS (2019) Dynamic interaction between basin redox and the biogeochemical nitrogen cycle in an unconventional Proterozoic petroleum system. *Scientific Reports,* **9**, 1-11.

Doyle KA, Poulton SW, Newton RJ, Podkovyrov VN, Bekker A (2018) Shallow water

anoxia in the Mesoproterozoic ocean: Evidence from the Bashkir Meganticlinorium, Southern Urals. *Precambrian Research,* **317**, 196-210.
Emerson S, Hedges J (1988) Processes controlling the organic carbon content of open ocean sediments. *Paleoceanography,* **3**, 621-634.
Ernst RE, Pease V, Puchkov VN, Kozlov VI, Sergeeva ND, Hamilton M (2006) Geochemical characterization of Precambrian Magmatic Suites of the Southeastern Margin of the East European Craton, Southern Urals, Russia. In: *Collection of Geologic Works*. Inst. Geol., Ufa, pp. 119–161 [in Russian].
Fawcett SE, Lomas MW, Casey JR, Ward BB, Sigman DM (2011) Assimilation of upwelled nitrate by small eukaryotes in the Sargasso Sea. *Nature Geoscience,* **4**, 717-722.
Frei R, Villa IM, Nagler TF, Kramers JD, Przybylowicz WJ, Prozesky VM, Hofmann BA, Kamber BS (1997) Single mineral dating by Pb–Pb stepleaching method: Assessing the mechanisms. *Geochimica et Cosmochimica Acta,* **61**, 393-414.
Freudenthal T, Wagner T, Wenzhoefer F, Zabel M, Wefer G (2001) Early diagenesis of organic matter from sediments of the eastern subtropical Atlantic: evidence from stable nitrogen and carbon isotopes. *Geochimica et Cosmochimica Acta,* **65**, 1795-1808.
Gilleaudeau GJ, Kah LC (2015) Heterogeneous redox conditions and a shallow chemocline in the Mesoproterozoic ocean: evidence from carbon–sulfur–iron relationships. *Precambrian Research*, **257**, 94-108.
Gilleaudeau GJ, Sahoo SK, Ostrander CM, Owens JD, Poulton SW, Lyons TW, Anbar A (2020) Molybdenum isotope and trace metal signals in an iron-rich Mesoproterozoic ocean: A snapshot from the Vindhyan Basin, India. *Precambrian Research*, doi: 10.1016/j.precamres.2020.105718.
Glasmacher UA, Bauer W, Clauer N, Puchkov VN (2004) Neoproterozoic metamorphism and deformation at the southeastern margin of the East European Craton, Uralides, Russia. *International Journal of Earth Sciences,* **93**, 921-944.
Glass JB, Wolfe-Simon F, Anbar AD (2009) Coevolution of metal availability and nitrogen assimilation in cyanobacteria and algae. *Geobiology,* **7**, 100-123.
Gruber N, Deutsch CA (2014) Redfield's evolving legacy. *Nature Geoscience,* **7**, 853-855.
Hardisty DS, Lu Z, Bekker A, Diamond CW, Gill BC, Jiang G, Kah LC, Knoll AH, Loyd SJ, Osburn MR, Planavsky NJ (2017) Perspectives on Proterozoic surface ocean redox from iodine contents in ancient and recent carbonate. *Earth and Planetary Science Letters*, **463**, 159-170.
Hiatt EE, Pufahl PK, Edwards CT (2015) Sedimentary phosphate and associated fossil bacteria in a Paleoproterozoic tidal flat in the 1.85 Ga Michigamme Formation, Michigan, USA. *Sedimentary Geology*, **319**, 24-39.
Hoch MP, Fogel ML, Kirchman DL (1992) Isotope fractionation associated with ammonium uptake by a marine bacterium. *Limnology and Oceanography*, **37**, 1447-1459.
Holland HD (1984) *The chemical evolution of the atmosphere and oceans,* Princeton University Press, Princeton, NJ.
Ilyin AV (1998) Rare-earth geochemistry of "old" phosphorites and probability of syngenetic precipitation and accumulation of phosphate. *Chemical Geology,* **144**, 243-256.
Karl DM, Bidigare RR, Letelier RM (2001) Long-term changes in plankton community structure and productivity in the North Pacific Subtropical Gyre: the domain shift hypothesis. *Deep Sea Research Part II: Topical Studies in Oceanography,* **48**, 1449-1470.
Karstensen J, Stramma L, Visbeck M (2008) Oxygen minimum zones in the eastern tropical Atlantic and Pacific oceans. *Progress in Oceanography,* **77**, 331-350.
Kholodov VN (1997) Epochs of Phosphorite Formation and Biogeochemistry of

Phosphorites. *Lithology and Mineral Resources,* **32**, 491-504.
Kipp MA, Lepland A, Buick R (2020) Redox fluctuations, trace metal enrichment and phosphogenesis in the ~2.0 Ga Zaonega Formation. *Precambrian Research*, doi: 10.1016/j.precamres.2020.105716.
Kipp MA, Stüeken EE (2017) Biomass recycling and Earth's early phosphorus cycle. *Science Advances,* **3**, doi: 10.1126/sciadv.aao4795.
Kipp MA, Stüeken EE, Yun M, Bekker A, Buick R (2018) Pervasive aerobic nitrogen cycling in the surface ocean across the Paleoproterozoic Era. *Earth and Planetary Science Letters,* **500**, 117-126.
Knoll AH, Nowak MA (2017) The timetable of evolution. *Science Advances,* **3**, doi: 10.1126/sciadv.1603076.
Koehler MC, Stüeken EE, Hillier S, Prave AR (2019) Limitation of fixed nitrogen and deepening of the carbonate-compensation depth through the Hirnantian at Dob's Linn, Scotland. *Palaeogeography, Palaeoclimatology, Palaeoecology,* **534**, doi: 10.1016/j.palaeo.2019.109321.
Koehler MC, Stüeken EE, Kipp MA, Buick R, Knoll AH (2017) Spatial and temporal trends in Precambrian nitrogen cycling: a Mesoproterozoic offshore nitrate minimum. *Geochimica et Cosmochimica Acta*, **198**, 315-337.
Kritee K, Sigman DM, Granger J, Ward BB, Jayakumar A, Deutsch C (2012) Reduced isotope fractionation by denitrification under conditions relevant to the ocean. *Geochimica et Cosmochimica Acta,* **92**, 243-259.
Krupenin MT (1999) Formation Environment of Siderites in the Lower Riphean Bakal Formation (the Southern Urals) [in Russian]. *Uralian Division RAS, Yekaterinburg*.
Kuznetsov AB, Bekker A, Ovchinnikova GV, Gorokhov IM, Vasilyeva IM (2017) Unradiogenic strontium and moderate-amplitude carbon isotope variations in early Tonian seawater after the assembly of Rodinia and before the Bitter Springs Excursion. *Precambrian Research,* **298**, 157-173.
Kuznetsov AB, Krupenin MT, Ovchinnikova GV, Gorokhov IM, Maslov AV, Kaurova OK, Ellmies R (2005) Diagenesis of carbonate and siderite deposits of the Lower Riphean Bakal Formation, the Southern Urals: Sr isotopic characteristics and Pb–Pb age. *Lithology and Mineral Resources,* **40**, 195-215.
Kuznetsov AB, Ovchinnikova GV, Gorokhov IM, Letnikova EF, Kaurova OK, Konstantinova GV (2013) Age constraints on the Neoproterozoic Baikal Group from combined Sr isotopes and Pb-Pb dating of carbonates from the Baikal type section, southeastern Siberia. *Journal Asian Earth Sciences,* **62**, 51-66.
Kuznetsov AB, Ovchinnikova GV, Semikhatov MA, Gorokhov IM, Kaurova OK, Krupenin MT, Vasileva IM, Gorokhovskii BM, Maslov AV (2008) The Sr isotopic characterization and Pb-Pb age of carbonate rocks from the Satka Formation, the Lower Riphean Burzyan Group of the southern Urals. *Stratigraphy and Geological Correlation*, **16**, 120-137.
Kuznetsov AB, Semikhatov MA, Gorokhov IM (2014) The Sr isotope chemostratigraphy as a tool for solving stratigraphic problems of the Upper Proterozoic (Riphean and Vendian). *Stratigraphy and Geological Correlation,* **22**, 553-575.
Kuznetsov AB, Vasilieva IM, Sitkina DR, Smirnova ZB, Kaurova OK (2018) Age of Carbonates and Phosphorites in the Sedimentary Cover of the Tuva–Mongolian Microcontinent. *Doklady Earth Sciences,* **479**, 282-285.
Lam P, Kuypers MM (2011) Microbial nitrogen cycling processes in oxygen minimum zones. *Annual Rreview of Marine Science,* **3**, 317-345.
Lehman MR, Bernasconi SM, Barbieri A, McKenzie JA (2002) Preservation of organic matter and alteration of its carbon and nitrogen isotope composition during simulated

and in situ early sedimentary diagenesis. *Geochimica et Cosmochimica Acta,* **66**, 3573-3584.

Lenton TM, Boyle RA, Poulton SW, Shields-Zhou GA, Butterfield NJ (2014) Co-evolution of eukaryotes and ocean oxygenation in the Neoproterozoic era. *Nature Geoscience,* **7**, 257-265.

Lepland A, Joosu L, Kirsimäe K, Prave AR, Romashkin AE, Črne AE, Martin AP, Fallick AE, Somelar P, Üpraus K, Mänd K (2014) Potential influence of sulphur bacteria on Palaeoproterozoic phosphogenesis. *Nature Geoscience,* **2014**, 20-24.

Lipschultz F, Wofsy SC, Ward BB, Codispoti LA, Friedrich G, Elkins JW (1990) Bacterial transformations of inorganic nitrogen in the oxygen-deficient waters of the Eastern Tropical South Pacific Ocean. *Deep Sea Research Part A: Oceanographic Research Papers,* **37**, 1513-1541.

Ludwig KR (2003) *User's manual for Isoplot/Ex, version 3.00, a geochronological toolkit for Microsoft Excel,* Berkeley Geochronology Center.

Lyons TW, Reinhard CT, Planavsky NJ (2014) The rise of oxygen in Earth's early ocean and atmosphere. *Nature,* **506**, 307-315.

Martin JH, Knauer GA, Karl DM, Broenkow WW (1987) VERTEX: carbon cycling in the northeast Pacific. *Deep-Sea Research,* **34**, 267-285.

Maslov AV (2004) Riphean and Vendian sedimentary sequences of the Timanides adn Uralides, the eastern periphery of the East European Craton. In: *The Neoproterozoic Timanide Orogen in Eastern Baltica* (eds Gee DG, Pease V). Geological Society, London, pp. 19-35.

Maslov AV, Erdtmann BD, Ivanov KS, Ivanov SN, Krupenin MT (1997) The main tectonic events, depositional history, and the palaeogeography of the Southern Urals during the Riphean-early Palaeozoic. *Tectonophysics,* **276**, 313-335.

Maslov AV, Krupenin MT, Gareev EZ, Anfimov LV (2001) *The Riphean of the Southern Urals Western Flank: Classical Sections, Sedimentology, Lithogenesis, Minerageny, Natural Geological Monuments [in Russian],* IGG URO RAS, Yekaterinburg.

McArthur JM, Tyson RV, Thomson J, Mattey D (1992) Early diagenesis of marine organic matter: Alteration of the carbon isotopic composition. *Marine Geology,* **105**, 51-61.

Müller PJ (1977) CN ratios in Pacific deep-sea sediments: Effect of inorganic ammonium and organic nitrogen compounds sorbed by clays. *Geochimica et Cosmochimica Acta,* **41**, 765-776.

Ovchinnikova GV, Kuznetsov AB, Melezhik VA, Gorokhov IM, Vasilyeva IM, Gorokhovskii BM (2007) Pb–Pb age of Jatulian carbonate rocks: the Tulomozero Formation of Southeast Karelia. *Stratigraphy and Geological Correlation,* **15**, 359-372.

Ovchinnikova GV, Kuznetsov AB, Vasil'eva IM, Gorokhov IM, Krupenin MT, Maslov AV, Turchenko TL (2008) Pb–Pb Age of Sedimentary Phosphorite Reworking in Lower Riphean Carbonate Sediments, the Satka Formation of Southern Urals. *Stratigraphy and Geological Correlation,* **16**, 138-142.

Ovchinnikova GV, Kuznetsov AB, Vasil'eva IM, Gorokhov IM, Letnikova EF, Gorokhovskii BM (2012) U-Pb age and Sr isotope signature of cap limestones from the Neoproterozoic Tsagaan Oloom Formation, Dzabkhan River basin, Western Mongolia. *Stratigraphy and Geological Correlation,* **20**, 516-527.

Ovchinnikova GV, Kuznetsov AB, Vasileva IM, Gorokhov IM, Krupenin MT, Gorokhovskii BM, Maslov AV (2013) Pb-Pb age and Sr isotopic characteristic of the Middle Riphean phosphorite concretions: the Zigaza-Komarovo Formation of the South Urals. *Doklady Earth Sciences,* **451**, 198-802.

Ovchinnikova GV, Vasilyeva IM, Semikhatov MA, Gorokhov IM, Kuznetsov AB,

Gorokhovskii BM, Levskii LR (2000) The Pb-Pb trail dating of carbonates with open U-Pb systems: the Myn'yar Formation of the Upper Riphean stratotype, southern Urals. *Stratigraphy and Geological Correlation,* **8**.

Ovchinnikova GV, Vasilyeva IM, Semikhatov MA, Kuznetsov AB, Gorokhov IM, Gorokhovskii BM, Levskii LK (1998) U-Pb systematics of Proterozoic carbonate rocks: the Inzer Formation of the Upper Riphean stratotype (Southern Urals). *Stratigraphy and Geological Correlation,* **6**, 336-347.

Papineau D (2010) Global biogeochemical changes at both ends of the Proterozoic: insights from phosphorites. *Astrobiology,* **10**, 165-181.

Planavsky NJ, McGoldrick P, Scott CT, Li C, Reinhard CT, Kelly AE, Chu X, Bekker A, Love GD, Lyons TW (2011) Widespread iron-rich conditions in the mid-Proterozoic ocean. *Nature,* **477**, 448-451.

Planavsky NJ, Reinhard CT, Wang X, Thomson D, McGoldrick P, Rainbird RH, Johnson T, Fischer WW, Lyons TW (2014) Low Mid-Proterozoic atmospheric oxygen levels and the delayed rise of animals. *Science,* **346**, 635-638.

Planavsky NJ, Slack JF, Cannon WF, O'Connell B, Isson TT, Asael D, Jackson JC, Hardisty DS, Lyons TW, Bekker A (2018) Evidence for episodic oxygenation in a weakly redox-buffered deep mid-Proterozoic ocean. *Chemical Geology,* **483**, 581-594.

Poulton SW, Canfield DE (2011) Ferruginous conditions: a dominant feature of the ocean through Earth's history. *Elements,* **7**, 107-112.

Poulton SW, Fralick PW, Canfield DE (2004) The transition to a sulphidic ocean ~1.84 billion years ago. *Nature,* **431**, 173-177.

Poulton SW, Fralick PW, Canfield DE (2010) Spatial variability in oceanic redox structure 1.8 billion years ago. *Nature Geoscience,* **3**, 486-490.

Premuzic ET, Benkovitz CM, Gaffney JS, Walsh JJ (1982) The nature and distribution of organic matter in the surface sediments of world oceans and seas. *Organic Geochemistry,* **4**, 63-77.

Pufahl PK, Groat LA (2017) Sedimentary and igneous phosphate deposits: formation and exploration: an invited paper. *Economic Geology,* **112**, 483-516.

Pushkov VN (1997) Structure and geodynamics of the Uralian orogen. In: *Orogeny Through Time* (eds Burg J-P, Ford M). Geological Society Special Publication, pp. 201-236.

Redfield AC (1934) On the Proportions of Organic Derivatives in Sea Water and Their Relation to the Composition of Plankton. In: *James Johnstone Memorial Volume*. University Press of Liverpool, pp. 176-192.

Reinhard CT, Planavsky NJ, Gill BC, Ozaki K, Robbins LJ, Lyons TW, Fischer WW, Wang C, Cole DB, Konhauser KO (2017) Evolution of the global phosphorus cycle. *Nature,* **541**, 386-389.

Robinson RS, Kienast M, Albuquerque AL, Altabet M, Contreras S, De Pol Holz R, Dubois N, Francois R, Galbraith E, Shu T-C, Ivanochko T, Jaccard S, Kao S-J, Kiefer T, Kienast S, Lehmann M, Martinez P, McCarthy M, Moebius J, Pedersen T, Quan TM, Ryabenko E, Schmittner A, Schneider R, Schneider-Mor A, Shigemitsu M, Sinclair D, Somes C, Studer A, Thunell R, Yang J-Y (2012) A review of nitrogen isotopic alteration in marine sediments. *Paleoceanography,* **27**, doi: 10.1029/2012PA002321.

Ronkin YL, Maslov AV, Kazak AP, Lepikhina OP, Matukov DI (2007) The Lower–Middle Riphean boundary in the Southern Urals: New Isotopic U–Pb (SHRIMP II) constraints. *Dokl. Eath. Sciences,* **415**, 356-401.

Rosenfeld JK (1979) Ammonium adsorption in nearshore anoxic sediments. *Limnology and Oceanography,* **24**, 356-364.

Sánchez-Baracaldo P, Raven JA, Pisani D, Knoll AH (2017) Early photosynthetic eukaryotes inhabited low-salinity habitats. *Proceedings of the National Academy of Sciences,*

114, doi: 10.1073/pnas.1620089114.
Sayle KL, Brodie CR, Cook GT, Hamilton WD (2019) Sequential measurement of δ15N, δ13C and δ34S values in archaeological bone collagen at the Scottish Universities Environmental Research Centre (SUERC): a new analytical frontier. *Rapid Communications in Mass Spectrometry,* **33**, 1258-1266.
Schidlowski M (2001) Carbon isotopes as biogeochemical recorders of life over 3.8 Ga of Earth history: evolution of a concept. *Precambrian Research,* **106**, 117-134.
Schroeder PA, McLain AA (1998) Illite-smectites and the influence of burial diagenesis on the geochemical cycling of nitrogen. *Clay Minerals,* **33**, 539-546.
Schulz HN, Schulz HD (2005) Large sulfur bacteria and the formation of phosphorite. *Science,* **307**, 416-418.
Semikhatov MA, Kuznetsov AB, Chumakov NM (2015) Isotope age of boundaries between the general stratigraphic subdivisions of the Upper Proterozoic (Riphean and Vendian) in Russia: The evolution of opinions and the current estimate. *Stratigraphy and Geological Correlation,* **23**, 568-579.
Semikhatov MA, Kuznetsov AB, Maslov AV, Gorokhov IM, Ovchinnikova GV (2009) Stratotype of the Lower Riphean, the Burzyan Group of the Southern Urals: Lithostratigraphy, paleontology, geochronology, Sr-and C-isotopic characteristics of its carbonate rocks. *Stratigraphy and Geological Correlation,* **17**, 574-601.
Shanmugam KT, O'gara F, Andersen K, Valentine RC (1978) Biological nitrogen fixation. *Annual Review of Plant Physiology,* **29**, 263-276.
Sigman DM, Karsh KL, Casciotti KL (2009) Ocean process tracers: nitrogen isotopes in the ocean. In: *Encyclopedia of ocean science*. Elsevier, Amsterdam.
Slack JF, Grenne T, Bekker A (2009) Seafloor-hydrothermal Si-Fe-Mn exhalites in the Pecos greenstone belt, New Mexico, and the redox state of ca. 1720 Ma deep seawater. *Geosphere,* **5**, 302-314.
Slack JF, Grenne T, Bekker A, Rouxel OJ, Lindberg PA (2007) Suboxic deep seawater in the late Paleoproterozoic: evidence from hematitic chert and iron formation related to seafloor-hydrothermal sulfide deposits, central Arizona, USA. *Earth and Planetary Science Letters,* **255**, 243-256.
Sperling EA, Rooney AD, Hays L, Sergeev VN, Vorob'eva NG, Sergeeva ND, Selby D, Johnston DT, Knoll AH (2014) Redox heterogeneity of subsurface waters in the Mesoproterozoic ocean. *Geobiology,* **12**, 373-386.
Sperling EA, Wolock CJ, Morgan AS, Gill BC, Kunzmann M, Halverson GP, Macdonald FA, Knoll AH, Johnston DT (2015) Statistical analysis of iron geochemical data suggests limited late Proterozoic oxygenation. *Nature,* **523**, 451-454.
Stüeken EE (2013) A test of the nitrogen-limitation hypothesis for retarded eukaryote radiation: nitrogen isotopes across a Mesoproterozoic basinal profile. *Geochimica et Cosmochimica Acta,* **120**, 121-139.
Stüeken EE, Kipp MA, Koehler MC, Buick R (2016) The evolution of Earth's biogeochemical nitrogen cycle. *Earth Science Reviews,* **160**, 220-239.
Stüeken EE, Tino C, Arp G, Jung D, Lyons TW (2020) Nitrogen isotope ratios trace high-pH conditions in a terrestrial Mars analog site. *Science Advances,* **6**, doi: 10.1126/sciadv.aay3440
Sverdrup HU, Johnson MW, Fleming RH (1942) *The Oceans: Their physics, chemistry, and general biology*, Prentice Hall, New York.
Tesdal JE, Galbraith ED, Kienast M (2013) Nitrogen isotopes in bulk marine sediment: linking seafloor observations with subseafloor records. *Biogeosciences,* **10**, 101-118.
Thomazo C, Papineau D (2013) Biogeochemical cycling of nitrogen on the early Earth. *Elements,* **9**, 345-351.

Wang H, Zhang Z, Li C, Algeo TJ, Cheng M, Wang W (2020a) Spatiotemporal redox heterogeneity and transient marine shelf oxygenation in the Mesoproterozoic ocean. *Geochimica et Cosmochimica Acta*, **270**, 201-217.

Wang Z, Wang X, Shi X, Tang D, Stüeken EE, Song H (2020b) Coupled Nitrate and Phosphate Availability Facilitated the Expansion of Eukaryotic Life at Circa 1.56 Ga. *Journal of Geophysical Research - Biogeosciences*, doi: 10.1029/2019JG005487.

Zhang X, Sigman DM, Morel FM, Kraepiel AM (2014) Nitrogen isotope fractionation by alternative nitrogenases and past ocean anoxia. *Proceedings of the National Academy of Sciences*, **111**, 4782-4787.